Redox-labelled electrochemical aptasensors with nanosupported cancer cells

S. Li, Yannick Coffinier, C. Lagadec, Fabrizio Cleri, K. Nishiguchi, A. Fujiwara, T. Fujii, S.-H. Kim, Nicolas Clement

Redox-labelled Electrochemical Aptasensors with Nanosupported Cancer Cells

S. Li[1], Y. Coffinier[2], C. Lagadec[3], F. Cleri[2], K. Nishiguchi[4], A. Fujiwara[4], T. Fujii[1], S.-H. Kim[1] and N. Clément[1]

[1] IIS, LIMMS/CNRS-IIS IRL2820, The Univ. of Tokyo 4-6-1 Komaba, Meguro-ku Tokyo, 153-8505, Japan

[2] IEMN, CNRS UMR8520, Univ. Lille Avenue Poincaré, BP 60069, 59652 Villeneuve d'Ascq cedex, France

[3] Univ. Lille, CNRS, Inserm, CHU Lille, Centre Oscar Lambret, UMR9020 – UMR-S 1277 - Canther – Cancer Heterogeneity, Plasticity and Resistance to Therapies, F-59000 Lille, France

[4] NTT Basic Research Laboratories, NTT Corporation, 3-1, Morinosato-Wakamiya, Atsugi-shi, 243-0198, Japan

ABSTRACT

The transfer of redox-labelled bioelectrochemical sensors from proteins to cells is not straightforward because of the cell downward force issue on the surface of the sensors. In this paper, we introduce 20-nm-thick nanopillars to overcome this issue, in a well-controlled manner. We show on both molecular dynamics simulations and experiments that suspending cells a few nanometers above an electrode surface enables redox-labelled tethered DNA aptamer probes to move freely, while remaining at an interaction distance from a target membrane protein, i. e. epithelial cell adhesion molecule (EpCAM), which is typically overexpressed in cancer cells. By this nanopillar configuration, the interaction of aptamer with cancer cells is clearly observable, with 13 cells as the lower limit of detection. Nanoconfinement induced by the gap between the electrode surface and the cell membrane appears to improve the limit of detection and to lower the melting temperature of DNA aptamer hairpins, offering an additional degree of freedom to optimize molecular recognition mechanisms. This novel nanosupported electrochemical DNA cell sensor scheme including Brownian-fluctuating redox species opens new opportunities for the design of all-electrical sensors using redox-labelled probes.

KEYWORDS: Bioelectrochemistry, Aptasensors, Nanopillars, Brownian motion, Nanoconfinement.

1. Introduction

Cancer is still one of the main pathologies with a high probability of a negative prognosis in humans (Bray et al., 2018). One of the main causes of death for cancer patients is due to organ failure induced by metastasis development. The primary tumor spread through the body by generating the circulating tumor cells (CTCs), cancer cells within the blood vessel. In the search for a personalized, high-precision medicine, much effort has been directed in recent years toward realizing cancer detection transducers and lab-on-a-chip devices, which aim to be used in the implementation of new strategies for early cancer detection and treatment, e.g., by targeting circulating tumor DNA, cancer-produced exosomes, or rare CTCs (Nagrath et al., 2007; Alix-Panabieres and Pantel, 2014; Dutta et al., 2019). For example, the CellSearch system, which has been approved by the U.S. Federal Drug Administration, detects CTCs by immobilizing cells through antibodies targeting the epithelial cell adhesion molecule (EpCAM) expression on the cell membrane. The number of CTCs is predictive of a short patient survival for several cancers and may serve as a liquid biopsy to guide therapy. However, sensitivity limitations reduce the impact of this approach, as the EpCAM expression heterogeneity among the CTC population (Wit et al., 2016).

Sensors in development are typically based on physicochemical effects such as fluorescence, chemiluminescence, magnetic beads, calorimetry profiling, or electrochemistry (Chen et al., 2021; Gao et al., 2019; Xie et al., 2020; Jiang et al., 2017; Alafeef et al., 2020). This last method seems to be the most promising one. Generally speaking, electrochemical aptasensors are more attractive due to their ease of operation, high sensitivity, and portability (Hashkavayi et al., 2020; Chennit et al., 2017; Mathew et al., 2020). However, so far, the use of aptasensors for cancer cells detection has been

restricted to label-free aptamer probes (Hashkavayi et al., 2021; Li et al., 2019; Sun et al., 2018). Another class of electrochemical sensors is based on redox-labelled aptamers, it is a very attractive alternative to successfully scale to micro or subcellar scale as every aptamer gives its contribution to the signal independently. However, the abundant literature on redox-labelled sensors established for protein or molecule detection (Chennit et al., 2017; Anne et al., 2011; Adjemian et al., 2010; Paiva et al., 2020; Torbensen et al., 2019; Xiao et al., 2007a; Xiao et al., 2007b; Zuo et al., 2009; Parolo et al., 2020), contrasts with the lack of studies at the cell level, which can be related downward forces (including gravity force and adhesive force) (Majhy et al., 2021) the sensor surface.

In this work, we used redox-labelled aptasensors targeting EpCAM protein, as a proof of concept, to study the electrochemical signal of immobilized cancer cells with dielectric nanopillars, as opposed to aptasensors with redox molecules in solution. In addition, we analyzed how the downward force of the cells affects the performance of the redox-labelled aptasensors. Moreover, the experimental results were compared with DNA molecular dynamics (MD) simulations by using the nanopillar supported cells configuration. Finally, the effects of nanoconfinement on the limit of detection (LOD) and the melting temperature of the aptamers were evaluated.

2. Materials and Methods

2.1 Fabrication of hydrogen silsesquioxane (HSQ) nanopillars

A HSQ (Dow Corning XR-1541) negative electron beam (e-beam) resist was used to fabricate the nanopillars by using high-speed e-beam lithography (Clément et al., 2011; Trasobares et al., 2016), with an Advantest F7000s-VD02 e-beam. Au (20 nm)/Ti (2

nm)/Si substrate was cleaned in acetone under sonication for 5 min, followed by rinsing with isopropyl alcohol and deionized water, and finally dried with nitrogen gas. The HSQ resin in a carrier solvent of methyl isobutyl ketone was spin-coated on the substrate with a speed of 5000 rpm for 60 s and then baked at 150 °C for 2 min on a hot plate. The cured sample was exposed to a dose of 500 μC/cm^2, and finally immersed in the alkaline developer NMD-3 (2.38% tetramethylammonium hydroxide) with agitation of 25 rpm for 5 min and then cured at 150 °C for 5 min to obtain the desired nanopillar array.

2.2 SYL3C Aptamer

Single-strand DNA SYL3C aptamer with 48nt length was originally synthesized through Systematic Evolution of Ligands Exponential enrichment (SELEX) methods by *Song et al.*, that showed high affinity (the K_d values of the SYL3C aptamer against breast cancer cell line MDA-MB-231 and Kato III cells were found to be 38 ± 9 and 67 ± 8 nM) and specificity to bind with EpCAM tested with a cell mixture in cell media (Song et al., 2013; Zhu et al., 2022; Li et al., 2022; Zhang et al., 2021; Wang et al. 2021; Sun et al., 2020, Ding et al. 2020). An interesting feature of this aptamer is that three hairpin structures were found to be essential binding site on EpCAM, which is different from that of EpCAM antibody. In this study, the sequence and modification of the aptamer was as follows: Ferrocene (Fc)-5′-CAC TAC AGA GGT TGC GTC TGT CCC ACG TTG TCA TGG GGG GTT GGC CTG-$(CH_2)_3$-3′-Thiol (SH) (purchased from Biomers).

2.3 Preparation of aptamer/oligoethylene glycol (OEG) mixed monolayers

The cleaned substrate with nanopillars was immersed in the freshly prepared solution of 1 mM thiolated OEG (OEG-SH) (containing an ethylene glycol repeat unit

$SH(CH_2)_3(OCH_2CH_2)_6OCH_2COOH$, purchased from Prochimia) in pure ethanol for 1 h and cleaned with ethanol. Then the chip was immersed in 1 μM SYL3C aptamer modified with thiol and Fc dissolved in 0.5 M potassium phosphate solution (pH 8) for X h (where X is 0.5 h, 1 h, 1.5 h, 2 h, 2.5 h, 3 h, 15 h) to obtain the mixed monolayers, following a similar approach introduced by Herne *et al*. (Herne and Tarlov, 1997) but with OEG-SH instead of mercapto-hexanol. Such an approach aimed to obtain a surface coverage as complete as possible that combines DNA with small molecules to avoid any DNA desorption arising from the oxidation of thiol bonds. The OEG backfilling approach is also known to drastically reduce biofouling and thus nonspecific protein adsorption (Dai et al., 2014).

The Cyclic Voltammetry (CV) was used to monitor the assembly process, shown in S1.1 and Figure S1. 2 h aptamer grafting time was considered as the optimum condition for high enough peak amplitude (I_{peak}) without too much packing aptamers on the electrode surface. The density of the aptamers was estimated to be about 2×10^{13} aptamers/cm^2. The CV curves (CVs) of one aptasensor up to 14 days and 10 different aptasensors are shown in Figure S2, the coefficient of variation for the stability and reproducibility is ±9% and ±3%, respectively. Monolayers composed of only DNA led to poor stability performances in CVs (Figure S3). The chip was cleaned with a solution of 0.05% Tween 20 for 10 s before use.

2.4 Detection of cells

The details were displayed in supplementary materials S1.1, S1.2 and S1.3.

2.5 Temperature control

Temperature control is applied directly from the bottom of the silicon chip with a hot plate (via a PCB card). The highly doped silicon and gold layer have good thermal conductivity to control the temperature in a few nanometers above the surface.

~~2.5~~ 2.6 MD simulations

Two types of MD simulations (coarse-grained and all-atom) were used for temperature and confinement dependent hydrogen-bond energy estimation (Fig.4) and molecular recognition respectively. Details are available in supplementary materials S1.4.

3. Results and discussion

3.1 Design of the redox-labelled aptasensor with nanopillars

The structure of the proposed device is shown in Figure 1. It is composed of 1) a gold working electrode (WE); 2) an active monolayer, composed of tethered Fc-labelled DNA aptamers and backfilling of OEG molecules; 3) a regular array of HSQ nanopillars. The HSQ solution is cross-linked to form a SiOx network structure after the e-beam exposure, providing a chemically stable, flat, and biocompatible pattern (Siegfried et al., 2011; del Campo and Arz, 2008). A diameter of 200 nm for the pillars was chosen to avoid any penetration through the cell membrane. The pitch and height of the pillars depend on the cell deformation between the pillars as well as the length of the aptamers (median of ~15 nm). A pillar height of 20 nm was primarily used for this study, but it was also tuned as discussed below. A pitch of 500 nm was chosen as a good compromise between a dense pillar array, enabling uniform cell penetration (Zhou et al., 2018), and a small increase in the nonfaradic/faradic current ratio (~10%, the pillar footprint only contributes to the nonfaradic current). The atomic force microscopy

(AFM) image shown in Figure 1c presents the nanopillars configuration, this configuration aimed to keep the cells at a distance z_{gap} of a few nanometers above the surface, which is small enough to enable an interaction between aptamers and EpCAM. Thiol bonds are formed on gold but not on HSQ pillars.

A simple description of the operation of this redox-labelled aptasensor is as follows: in the presence of nontarget cells, the aptamers move freely, and electron transfer between the surface and redox markers is allowed (Figure 1a). In contrast, electron transfer to the redox marker is blocked when the aptamers bind to EpCAM (Figure 1b). The expected CVs are shown in Figure 1d. Given the simple nature of the structure under study, MD simulations can be used to support the analysis of the experimental results, as discussed below.

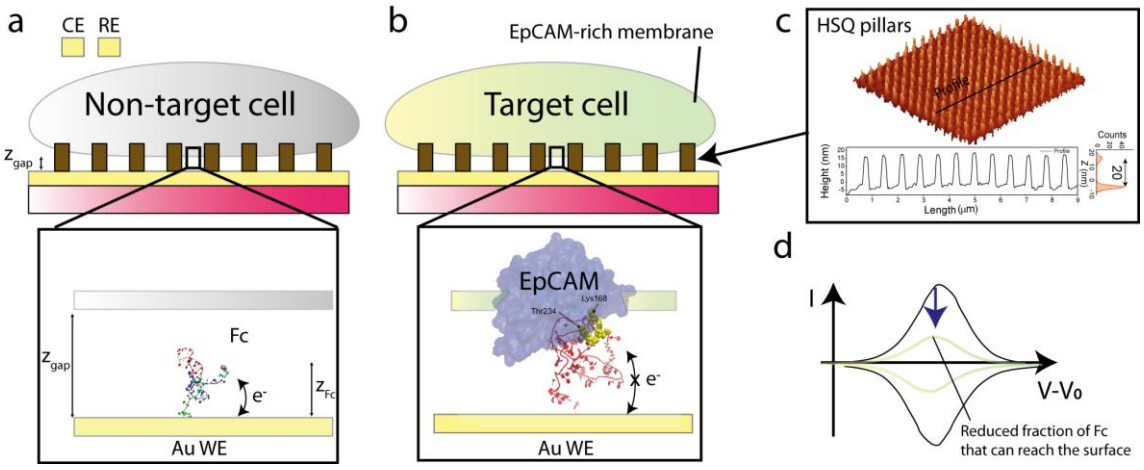

Figure 1. (a) Schematic representation of the device composed of a WE bearing nanopillars, a tethered and redox-labelled SYL3C aptamer, a counter electrode (CE) and

a reference electrode (RE-3VT). (b) Schematic representation of the device used for the molecular recognition of EpCAM on a target cell. (c) AFM image (10μm × 10μm) and AFM cross section of the HSQ nanopillars. (d) Schematic representation of the typical CVs of redox-labelled aptasensors.

3.2 Detection of the target cells on the nanostructured chip

Figure 2a shows the control experiment of the device without nanopillars in the absence/presence of the lymphoma cell line Ramos, which does not express EpCAM (Xie et al., 2016). Although no molecular recognition was expected in this configuration, the I_{peak} decreased 51%. In the case of pancreatic cancer cells (Capan-2), which have a high level of EpCAM expression (Mayado et al., 2020), a larger decrease of I_{peak} (63%) was observed (Figure 2c), showing the effective molecular recognition. The shift of I_{peak} in the control experiment was attributed to a cell downward force effect. The cells are pushing water molecules away, it induces the potential at the monolayer interface is different from the one in solution, this effect is similar to the "current blocking" effect exploited in some label-free electrochemical biosensors (Mathew et al., 2020). To solve this issue, the nanopillar arrays were introduced. Figure 2b shows the control experiment by using nanostructured chip, with an unchanged I_{peak} in the presence of Ramos cells. In contrast, the I_{peak} was decreased (43%) when Capan-2 cells were inserted (Figure 2d).

For better understanding of the charge transfer mechanisms in the absence/presence of target EpCAM, a series of all-atom MD simulation was performed (Cleri and Rosato, 1993; Cleri et al., 2021). When the aptamer does not interact with EpCAM, Fc moves freely and has chances to be in close proximity from the surface (Figure S4a,

supplementary Movie). However, when the aptamer is partly bound to the EpCAM, Fc is either blocked or remains too far from the surface to enable electron transfer (Figure S4a). As a result, only aptamers that do not interact with EpCAM do contribute to the current and I_{peak} decrease can be related to the percentage of aptamers interacting with the cell. We stress that SYL3C aptamer/EpCAM interaction is thermally activated as related to the formation of H-bonds, notably the Lys168 and the Thr234 (Figure 1b, Figure S4b).

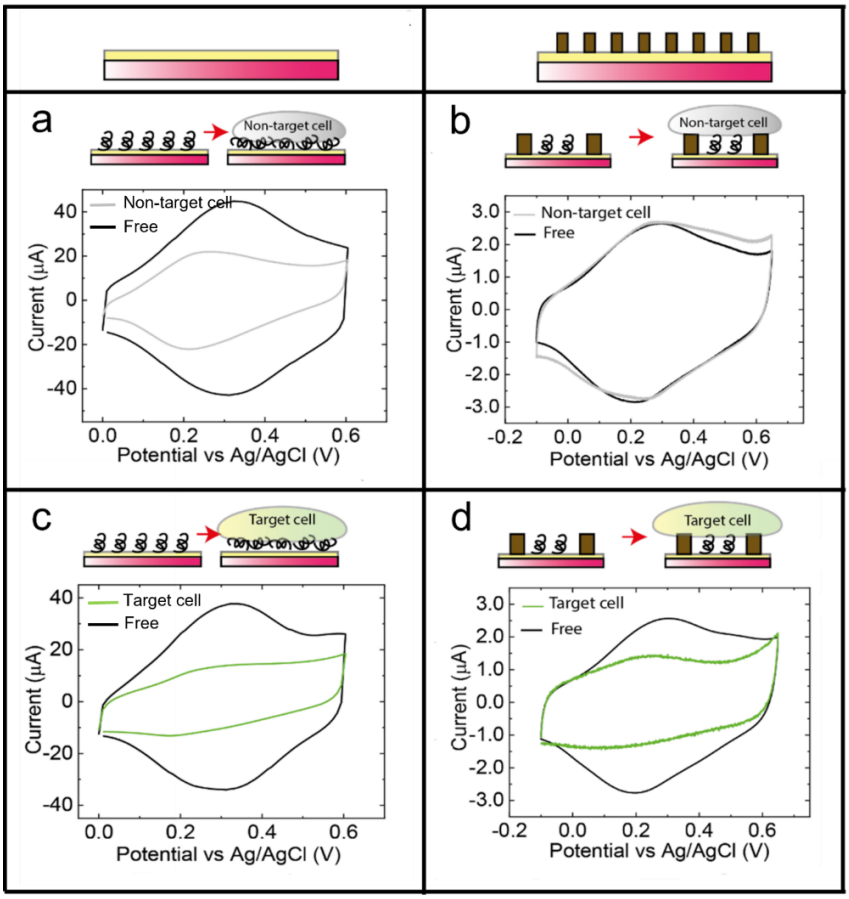

Figure 2. (a) CVs (scan rate v = 0.5 V/s) of a device without nanopillars in the presence/absence of nontarget cells. (b) CVs (v = 0.05 V/s) of a device with nanopillars in the presence/absence of nontarget cells. (c) CVs (v = 0.5 V/s) of a device without

nanopillars in the presence/absence of target cells. (d) CVs (v = 0.05 V/s) of a device with nanopillars in the presence/absence of target cells.

3.3 LOD of the nanostructured chip

This nanostructured chip with SYL3C aptamer showed an excellent selectivity and logarithmic sensor response to Capan-2 cells, spreading over two orders of magnitude (Figure 3). It was observed that the CV peaks decreased with the increase of Capan-2 concentrations within the range from 25 to 5000 cells (corresponding to 5×10^3 cells/mL to 1×10^6 cells/mL). The number of the cells for each concentration was estimated by the volume of the buffer in the microfluidic channel and verified by fluorescent microscopy (Figure S5). By fitting the extracted oxidized I_{peak} from Figure 3a, with $I = 7.567 - 0.995 \times log\ C\ cells$ (cells/mL) and a coefficient of determination $R^2 = 0.964$, LOD was calculated to be 13 cells, relative standard deviations (RSD% < 6%) (see supplementary S1.5 for details). Besides, a cell mixture was considered including Ramos cells at fixed concentration of 5×10^4 cells/mL and a variable concentration of Capan-2 cells (5×10^3 cells/mL to 1×10^6 cells/mL) for the device selectivity (CVs are shown in Figure S6), I_{peak}, plotted in green color in Figure 3b, is fitted with $I = 7.123 - 0.829 \times log\ C$ (cells/mL) and $R^2 = 0.938$, which corresponds to a LOD of 15 cells. The logarithmic dependence of I_{peak} with C can be related to the presence of cell clusters (Figure S5) following the Brunauer, Emmett, and Teller adsorption model (Brunauer et al., 1938), as well as the slightly different slope observed in the case of a mixture of cells.

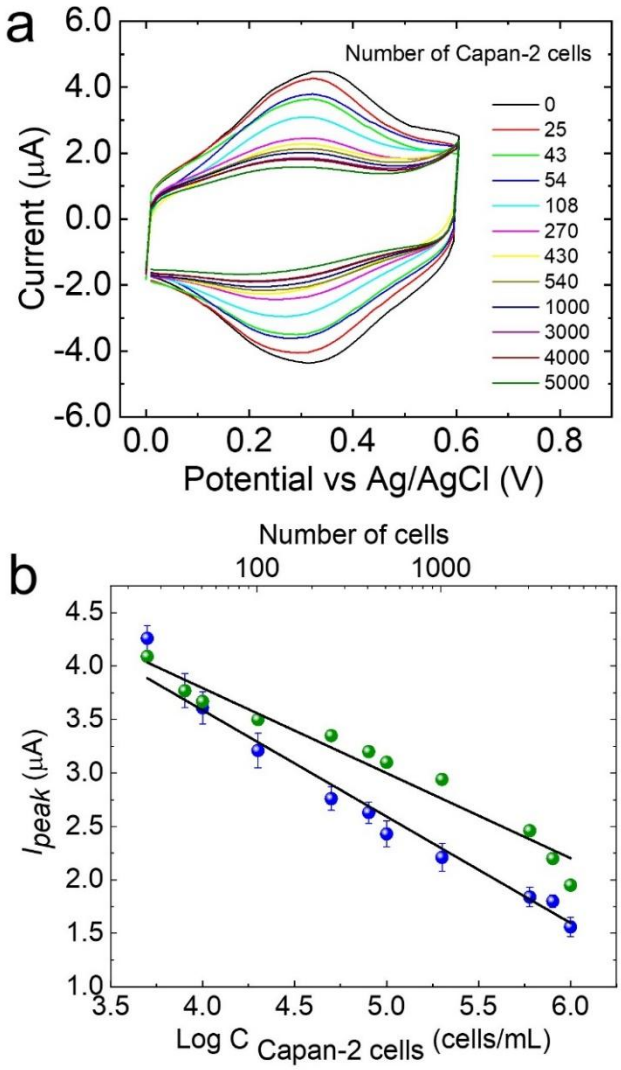

Figure 3. (a) CVs (v = 0.1 V/s) obtained for different concentrations of Capan-2 cells. (b) I_{peak} extracted from (a) in blue color and from Figure S6 in green color is plotted as a function of the Capan-2 cell concentration (log-scale) and the number of cells. Error bars: ± standard deviation (SD), samples n = 3, corresponding to experiments performed with 3 different devices.

3.4 Aptamer Brownian motion: nanoconfinement effect

The possibility of suppressing the cell downward force effect offers additional opportunities. For example, the simplicity of the molecular assembly, the nanopillar configuration enables a direct link between the experimental results and the MD simulations. By noticing that the cell downward force effect was observed with a nanopillar height of up to 17 nm (see AFM images in Figure S7 and related line scan in Figures 4a,b), such an experiment with different pillars height enable to evaluate cells deformation around pillars from the change in electrochemical signal and therefore to have a relatively quantitative idea of the nanogap for 20 nm-thick pillars. A monolayer thickness of about 2 nm and a value of z_{gap} = 5 nm were considered for the simulation. According to the computer simulations (Snodin et al., 2015), lateral nanoconfinement could afford a precious degree of freedom to tune the hairpin melting temperature. Figure 4c shows the hydrogen bond energy histogram and configurations for tethered SYL3C at different temperatures in the absence/presence of a 5 nm confinement. This energy is related to the number of base pairs formed and, therefore, to the various hairpin configurations (Yang et al., 2019; Boichuk et al., 2019). The unconfined tethered SYL3C showed three main peaks at 20 °C, whereas only low-energy peaks were observed above 40 °C, as expected from the SYL3C configurations with 3 and 1–2 hairpins, respectively. In contrast, the hydrogen bond energy distribution for tethered SYL3C under confinement only showed a configuration with low-energy peaks, suggesting a lower melting temperature due to the confinement effect.

Experimental measurements on tethered SYL3C have been performed with temperatures varying between 25 °C and 70 °C (Figure 4d). We expected that cells do not survive at elevated temperatures, but the EpCAM is still operational. Figure S8 shows the successful detection of EpCAM proteins at 70 degrees. Experimental results

show a weak temperature dependence (< ± 6%) for SYL3C under confinement with Ramos cells, a decrease of I_{peak} with temperature increase for unconfined SYL3C, and an even larger I_{peak} decrease for SYL3C with Capan-2 cells (CVs are shown in Figure S9). We propose the following mechanism, in agreement with MD simulations: for unconfined DNA, as the temperature is increased, the number of hairpins is reduced, which affects the DNA effective length. In addition, DNA stands up reducing the number of Fc that can transfer electrons at the interface (I_{peak} is decreased). In contrast, DNA cannot stand up under nanoconfinement. Therefore, for the control cells, they can transfer electrons at equilibrium because they can come close to the interface (I_{peak} is unchanged with the increase of temperature). For confined DNA (target cell), the aptamer is in the optimized hairpin configuration. Interaction with EpCAM is improved with temperature increase as the formation of hydrogen bonds is thermally activated, as mentioned above.

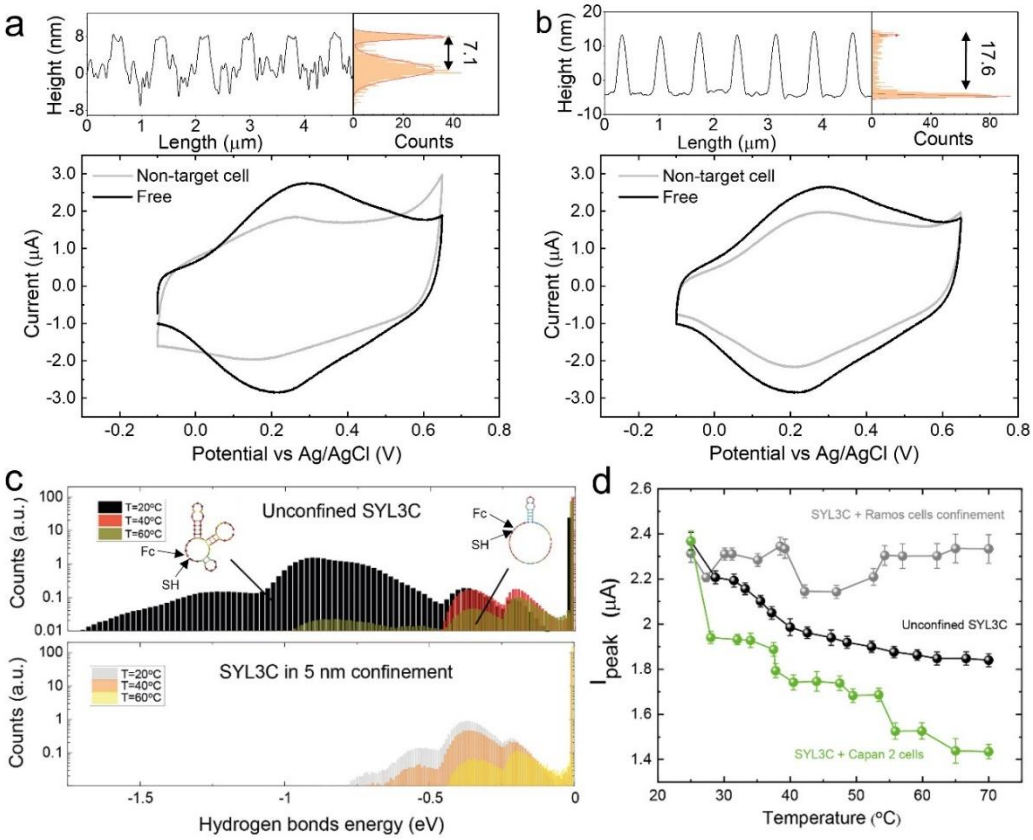

Figure 4. (a), (b) AFM cross section and CVs (v = 0.05 V/s) obtained for 7.1 nm and 17.6 nm nanopillars (with/without Ramos cell), respectively. (c) Hydrogen bond energy estimated from the MD simulation of tethered SYL3C without confinement and under 5 nm confinement. Inset, SYL3C hairpin configurations at 20 °C and 60 °C are obtained from Nupack software. (d) I_{peak} is plotted as a function of temperature for unconfined SYL3C (RSD% < 3%), confined SYL3C with Ramos cells (RSD% < 2%), and Capan-2 cells (RSD% < 4%). Error bars: ± SD, n = 3, corresponding to CVs performed 3 times on the same device.

3.5 Discussion on cell downward force, LOD, and temperature effects

Interestingly, previously reported electrochemical cytosensors are typically based on a more complex architecture involving several molecular self-assembly steps and

nanoparticles (Sun et al., 2018). One can argue that these nanoparticles, once on the surface, play an analogous role to our HSQ nanopillars presented here. However, the nanopillar approach could simplify the assembly process and presents a homogeneous surface thanks to the periodic pillar network, helping to perfectly control z_{gap}, while being compatible with the ultimate downscaling/integration with many nanoelectrodes. We stress that a variety of nanopatterned surfaces, including nanopillars, have been widely used to investigate the cellular functions on the surface of cells or to capture cells (Wang et al., 2014; Loeian et al., 2019; Sun et al, 2022; Cui et al., 2020). In these studies, nanopillars were typically in the hundreds of nanometers to micrometer range, as opposed to 20 nm in the present study, due to different objectives.

So far, electrochemical cytosensors based on label-free sensing have not reached the single-cell sensitivity (Sun et al., 2019). In our present study, the LOD (in number of cells) is about 13 cells. Future versions of the device will be developed in multiple electrode configurations, thus enabling statistical analysis at the single-cell level (or subcellular level to target multiple biomarkers), exploiting our single-cell trapping lab-on-a-chip (Kim et al., 2019), which additionally suppresses the cell clusters. With the cell downward force issue solved, the actual LOD is the nonfaradic capacitance arising from the sensing nanolayer, which is proportional to the active area. As 13 cells correspond to about 1/1000 of the active area in the present study, the use of the sensing area matching exactly to a single cell should enable a high faradic/nonfaradic ratio to be obtained. The absolute I_{peak} value is expected to be in the tens of pico-Amperes for a single cell, which could be measured with commercial equipment. Interestingly, the recent breakthrough in electrochemistry instrumentation allowing CVs at the atto-Ampere level for redox-labelled molecules would be directly beneficial to the present

sensing approach, granting subcellular studies with nanoelectrodes in the 10-nm range (Grall et al., 2021). Finally, this nano-supported cell approach could also be beneficial to nanowire based aptasensors (Kutovyi et al., 2020) for subcellular sensing.

A second advantage of this device is related to the temperature dependence associated with the confinement effect. These devices aim to be implemented at the single-cell level, providing statistical distributions related to target and nontarget cell populations. As a result, the relevant signal is $\Delta I_{peak} = I_{peak}$ (target cell) – I_{peak} (nontarget cell). According to Figure 4d, the difference in the signal ΔI_{peak} increased significantly with the temperature as the I_{peak} related to nontarget cells did not depend on the temperature. Additionally, the confinement-induced hairpin melting temperature reduction was clearly observed in the MD simulations for SYL3C and was consistent with experimental data. This effect has some similarities with the recent report of duplex weakening when duplex DNA is placed in a nanocage (Jonchhe et al., 2020). The exact underlying mechanism remains to be unveiled in future studies. We are currently investigating the nanoconfinement-induced polymer increased stiffness on tethered DNA using molecular touching AFM combined with scanning electrochemical microscopy (Chennit et al., 2017). Hairpin weakening under nanoconfinement is a very attractive characteristic of the SYL3C aptamer, and probably many other aptamers, because it stabilizes the aptamer in the optimum aptamer folded configuration corresponding to 37 °C that was obtained by the systematic evolution of ligands by exponential enrichment method (Song et al., 2013).

4. Conclusion

In conclusion, we demonstrated for the first time a redox-labelled aptasensor for cancer cell detection. This was achieved by using ~~that uses~~ nanopillar arrays to efficiently suppress the cell downward force issue. A LOD of 13 cells has been demonstrated for EpCAM expressed cancer cells as well as selectivity with a cell mixture. The MD analyses and experimental data have suggested that aptamer confinement significantly affects the aptamer melting temperature. Such an effect is a precious degree of freedom that can be used to stabilize the aptamer in the optimum configuration. This method is promising for realizing the next-generation device electrochemical devices for single-cell and potentially subcellular or single-molecule analysis.

AUTHOR INFORMATION

Corresponding Author

* Nicolas Clément, Email: nclement@iis.u-tokyo.ac.jp.

* Shuo Li, Email: shuoli06@iis.u-tokyo.ac.jp.

Author Contributions

S.L. fabricated the HSQ pillars; performed the self-assemblies, cell culture, and electrochemical measurements; analyzed the data; and co-wrote the paper. All co-authors supervised the work and contributed to writing the manuscript. The molecular dynamics simulations were performed by N.C. (oxDNA) and F.C. (full atomistic and docking).

Funding Sources

This work was funded by the Kakenhi project for foreign researchers [grant number: P19801] from the Japan Society for the Promotion of Science, and the projects ANR SIBI and CNRS MITI BIOSTAT.

ACKNOWLEDGMENTS

The authors thank Dr. E. Lebrasseur for his help with device fabrication, Dr. C. Demaille for discussion and Dr. L. Jalabert for support with atomic force microscopy characterization as well as advice for device fabrication.

REFERENCES

Bray, F., Ferlay, J., Soerjomataram, I., Siegel, R. L., Torre, L. A., Jemal, A., 2018. CA Cancer J. Clin. 68 (6), 394-424.

Nagrath, S., Sequist, L. V., Maheswaran, S., Bell, D. W., Irimia, D., Ulkus, L., Smith, M. R., Kwak, E. L., Digumarthy, S., Muzikansky, A., Ryan, P., Balis, U. J., Tompkins, R. G., Haber, D. A., Toner, M., 2007. Nature 450 (7173), 1235-1239.

Alix-Panabieres, C., Pantel, K. 2014. Nat. Rev. Cancer 14 (9), 623-631.

Dutta, R., Liba, O., SoRelle, E. D., Winetraub, Y., Ramani, V. C., Jeffrey, S. S., Sledge, G. W., de la Zerda, A., 2019. Nano Lett. 19 (4), 2334-2342.

Wit, S. D., Dalum, G. V., Lenferink, A. T. M., Tibbe, A. G. J., Hiltermann, T. J. N., Groen, H. J. M., Van Rijn, C. J. M., Terstappen, L. W. M. M., 2015. Sci. Rep. 5 (1), 12270.

Chen, P., Wang, Y., He, Y., Huang, K., Wang, X., Zhou, R., Liu, T., Qu, R., Zhou, J., Peng, W., Li, M., Bai, Y., Chen, J., Huang, J., Geng, J., Xie, Y., Hu, W. Ying, B., 2021. ACS Nano 15, 11634-11643.

Gao, J. W., Chen, M. M., Wen, W., Zhang, X., Wang, S., Huang, W. H., 2019. Nanoscale 11 (36), 16860-16867.

Xie, X., Zhang, L., Zhang, W., Tayebee, R., Hoseininasr, A., Vatanpour, H. H., Behjati, Z., Li, S., Nasrabadi, M., Liu, L., 2020. J. Mol. Liq. 309, 113024.

Jiang, Y., Shi, M., Liu, Y., Wan, S., Cui, C., Zhang, L., Tan, W., 2017. Angew. Chem. Int. Ed. 56 (39), 11916-11920.

Alafeef, M., Dighe, K., Moitra, P., Pan, D., 2020. ACS Nano 14, 17028-17045.

Hashkavayi, A. B, Cha, B. S., Lee, E. S., Kim, S., Park, K. S., 2020. Anal. Chem. 92 (19), 12733-12740.

Chennit, K., Trasobares, J., Anne, A., Cambril, E., Chovin, A., Clément, N., Demaille, C., 2017. Anal. Chem. 89 (20), 11061-11069.

Mathew, D. G., Beekman, P., Lemay, S. G., Zuilhof, H., Le Gac, S., van der Wiel, W. G., 2020. Nano Lett. 20 (2), 820-828.

Hashkavayi, A. B., Cha, B. S., Hwang, S. H., Kim, J., Park, K. S., 2021. Sens. and Actuators B: Chem. 343, 130087.

Li, J., Lin, X. F., Zhang, Z. Y., Tu, W.W., Dai, Z. H., 2019. Biosens. Bioelectron. 126, 332-338.

Sun, D., Lu, J., Luo, Z., Zhang, L., Liu, P, Chen, Z., 2018. Biosens. Bioelectron. 120, 8-14.

Anne, A., Chovin, A., Demaille, C., Lafouresse, M., 2011. Anal. Chem. 83 (20), 7924-7932.

Adjemian, J., Anne, A., Cauet, G., Demaille, C., 2010. Langmuir 26 (12), 10347-10356.

Paiva, T. O., Torbensen, K., Patel, A. N., Anne, A., Chovin, A., Demaille, C., Bataille, L., Michon, T., 2020. ACS Catal. 10 (14), 7843-7856.

Torbensen, K., Patel, A. N., Anne, A., Chovin, A., Demaille, C., Bataille, L., Michon, T., Grelet, E., 2019. ACS Catal. 9 (6), 5783-5796.

Xiao, Y., Lai, R. Y., Plaxco, K. W., 2007a. Nat. Protoc. 2 (11), 2875-2880.

Xiao, Y., Qu, X., Plaxco, K. W., Heeger, A. J., 2007b. J. Am. Chem. Soc. 129 (39), 11897.

Zuo, X. L., Xiao, Y., Kevin W., Plaxco, K. W., 2009. J. Am. Chem. Soc. 131 (20), 6944-6945.

Parolo, C., Greenwood, A. S., Ogden, N. E., Kang, D., Hawes, C., Ortega, G., Arroyo-Currás, N., Plaxco, K. W., 2020. Microsyst. Nanoeng. 6, 13.

Majhy, B., Priyadarshini, P., Sen, A. K., 2021. RSC Adv. 11, 15467-15476.

Clément, N., Patriarche, G., Smaali, K., Vaurette, F., Nishiguchi, K., Troadec, D., Fujiwara, A., Vuillaume, D., 2011. Small 7 (18), 2607-2613.

Trasobares, J., Rech, J., Jonckheere, T., Martin, T., Aleveque, O., Levillain, E., Diez-Cabanes, V., Olivier, Y., Cornil, J., Nys, J. P., Sivakumarasamy, R., Smaali, K., Leclere, P., Fujiwara, A., Théron, D., Vuillaume, D., Clément, N., 2016. Nat. Commun. 7, 12850.

Song, Y., Zhu, Z., An, Y., Zhang, W., Zhang, H., Liu, D., Yu, C., Duan, W., Yang, C. J., 2013. Anal. Chem. 85 (8), 4141-4149.

Zhu, L., Yang, J., Ma, Y., Zhu, X., Zhang, C., 2022. J. Am. Chem. Soc. 144 (4), 1493-1497.

Li, C., Yang, S., Li, R., Gong, S., Huang, M., Sun, Y., Xiong, G., Wu, D., Ji, M., Chen, Y., Gao, C., Yu, Y., 2022. ACS Appl. Mater. Interfaces 14 (6), 7646-7658.

Zhang, H. Yu, X. Liu, Y. Lin, B. Jiang, M. Song, J. Di, W. Zhu, Z. Yang, C., 2021. Anal. Chem. 93 (19), 7235-7241.

Wang, J., Xie, H., Ding, C., 2021. ACS Appl. Mater. Interfaces 13 (28), 32837-32844.

Sun, S., Yang, S., Hu, X., Zheng, C., Song, H., Wang, L., Shen, Z., Wu, Z. S., 2020 ACS Sens. 5 (12), 3870-3878.

Ding, P., Wang, Z., Wu, Z., Zhou, Y., Sun, N., Pei, R., 2020. ACS Appl. Mater. Interfaces 12 (18), 20263-20270.

Herne, T. M., Tarlov M. J., 1997. J. Am. Chem. Soc., 119 (38), 8916-8920.

Dai, Q., Walkey, C., Chan, W. C., 2014. Angew. Chem. Int. Ed. 53 (20), 5093-5096.

Siegfried, T., Ekinci, Y., Solak, H. H., Martin, O. J. F., Sigg, H., 2011. Appl. Phys. Lett. 99, 263302.

del Campo, A., Arz, E., 2008. Chem. Rev. 108, 911-945.

Zhou, J., Zhang, X., Sun, J., Dang, Z., Li, J., Li, X., Chen, T., 2018. Phys. Chem. Chem. Phys. 20 (35), 22946-22951.

Xie, X., Li, F., Zhang, H., Lu, Y., Lian, S., Lin, H., Gao, Y., Jia, L., 2016. Eur. J. Pharm. Sci. 83, 28-35.

Mayado, A., Orfao, A., Mentink, A., Gutierrez, M. L., Muñoz-Bellvis, L., Terstappen, L. W. M. M., 2020. Cancer Drug Resist. 3, 83-97.

Cleri, F., Rosato, V., 1993. Phys. Rev. B 48, 22-33.

Cleri, F, Lensink, M. F., Blossey, R., 2021. Front. Mol. Biosci. 8, 778.

Brunauer, S., Emmett, P. H., Teller, E., 1938. J. Am. Chem. Soc. 60 (2), 309-319.

Snodin, E. K. B., Randisi, F., Mosayebi, M., Šulc, P., Schreck, J. S., Romano, F., Ouldridge, T. E., Tsukanov, R., Nir, E., Louis, A. A., Doye1, J. P. K., 2015. J. Chem. Phys. 142, 234901.

Yang, H. W., Ju, S. P., Lin, Y. S., 2019. Comput. Struct. Biotechnol. J. 17, 812-820.

Boichuk, N., Kutovyi, Y., Lobato-Dauzier, N., Genot, A., Fujii, T., Offenhäusser, A., Vitusevich, S., Clément, N., 2019. International Conference on Noise and Fluctuations (ICNF 2019), EPFL Neuchâtel campus - Neuchâtel, Switzerland, 18-21 June.

Sun, D., Lu, J., Luo, Z., Zhang, L., Liu, P, Chen, Z., 2018. Biosens. Bioelectron. 120, 8-14.

Wang, S., Wan, Y., Liu, Y., 2014. Nanoscale 6 (21), 12482-12489.

Loeian, M. S., Mehdi Aghaei, S., Farhadi, F., Rai, V., Yang, H. W., Johnson, M. D., Aqil, F., Mandadi, M., Rai, S. N., Panchapakesan, B., 2019. Lab Chip 19 (11), 1899-1915.

Sun, N., Yang, Y., Miao, H., Redublo, P., Liu, H., Liu, W. Huang, Y. W., Teng, P. C., Zhang, C., Zhang, R. Y., Smalley, M., Yang, P., Chou, S. J., Huai, K., Zhang, Z., Lee, Y. T., Wang, J. J., Wang, J., Liang, I. Y., Zhang, T. X., Zhang, D., Liang, L., Weiss, P. S., Posadas, E. M., Donahue, T., Hecht, J. R., Allen-Auerbach, M. S., Bergsland, E. K., Hope, T. A., Pei, R., Zhu, Y., Tseng, H. R., Heaney, A. P., 2022. Biosens. Bioelectron. 199, 113854.

Cui, H., Liu, Q., Li, R., Wei, X., Sun, Y., Wang, Z., Zhang, L., Zhao, X. Z., Hua, B., Guo, S. S., 2020. Nanoscale 12 (3), 1455-1463.

Sun, D., Lu, J., Zhang, L., Chen, Z., 2019. Anal. Chim. Acta. 1082, 1-17.

Kim, S. H., Ito, H., Kozuka, M., Takagi, H., Hirai, M., Fujii, T., 2019. Lab Chip 19 (5), 757-766.

Grall, S., Alic, I., Pavoni, E., Awadein, M., Fujii, T., Mullegger, S., Farina, M., Clément, N., Gramse, G., 2021. Small 17 (29), 2101253.

Kutovyi, Y., Hlukhova, H., Boichuk, N., Menger, M., Offenhäusser, A., Vitusevich, S., 2020. Biosens. Bioelectron. 154, 112053.

Jonchhe, S., Pandey, S., Karna, D., Pokhrel, P., Cui, Y., Mishra, S., Sugiyama, H., Endo, M., Mao, H., 2020. J. Am. Chem. Soc. 142 (22), 10042-10049.